World Electric Vehicle Journal

MDPI

Article

Simulation and Experimental Study on Heat Transfer Performance of Bionic Structure-Based Battery Liquid Cooling Plate

Zhizhong Wang [1], Dinghong Liu [2], Zhaoyang Li [2], Xin Qi [2] and Chaoyi Wan [1,*]

[1] School of Automotive and Traffic Engineering, Jiangsu University of Technology, Changzhou 213001, China; 2022655124@smail.jsut.edu.cn
[2] CATARC Automotive Test Center (Changzhou) Co., Ltd., Changzhou 213001, China; liudinghong@catarc.ac.cn (D.L.)
* Correspondence: wcy@jsut.edu.cn

Abstract: This study presents a bionic structure-based liquid cooling plate designed to address the heat generation characteristics of prismatic lithium-ion batteries. The size of the lithium-ion battery is 148 mm × 26 mm × 97 mm, the positive pole size is 20 mm × 20 mm × 3 mm, and the negative pole size is 22 mm × 20 mm × 3 mm. Experimental testing of the Li-ion battery's heat generation model parameters, in conjunction with bionic structure and micro-channel features, has led to the development of this innovative cooling system. The traditional bionic liquid cooling plate's structure is often singular; however, the flow path of the liquid cooling plate designed in this paper is based on the combination of the distribution of human blood vessel branches and the structure of insect wing veins. The external dimension of the liquid cooling plate is 152 mm × 100 mm × 6 mm (length × width × height). Utilizing numerical simulation and thermodynamic principles, we analyzed the heat transfer efficacy of the bionic liquid cooling module for power batteries. Specifically, we investigated the impact of varying coolant flow rates and the contact radius between flow channels on the thermal performance of the bionic battery modules. Our findings indicate that a liquid flow rate of 0.6 m/s achieves a stable maximum surface temperature and temperature differential across the bionic battery liquid cooling module, with a relatively low overall system power consumption, suggesting room for further enhancement of heat transfer performance. By augmenting the contact radius between flow channels, we observed an initial increase in the maximum surface temperature, temperature differential, and inlet–outlet pressure differential at a flow rate of 0.2 m/s. However, at flow rates equal to or exceeding 0.4 m/s, these parameters stabilized across different design Scenarios. Notably, the pump power consumption remained consistent across various scenarios and flow rates. This study's outcomes offer valuable insights for the development of liquid-cooled battery thermal management systems that are energy-efficient and offer superior heat transfer capabilities.

Keywords: lithium-ion battery; bionic structure-based design; liquid cooling plate; numerical simulation; battery thermal management

Citation: Wang, Z.; Liu, D.; Li, Z.; Qi, X.; Wan, C. Simulation and Experimental Study on Heat Transfer Performance of Bionic Structure-Based Battery Liquid Cooling Plate. *World Electr. Veh. J.* **2024**, *15*, 464. https://doi.org/10.3390/wevj15100464

Academic Editor: Michael Fowler

Received: 16 August 2024
Revised: 16 September 2024
Accepted: 7 October 2024
Published: 12 October 2024

1. Introduction

Power batteries, as the power source of new energy vehicles, play a decisive role in the development of the new energy vehicle industry. There are many factors affecting the safety of batteries, with temperature being the most significant one. If the battery does not dissipate heat in time, it will lead to excessive battery temperature. In severe cases, it can cause thermal runaway, leading to accidents and even fatalities. Therefore, an efficient battery thermal management system (BTMS) is urgently needed to ensure that the operating temperature of the battery pack is within the range of 293.15–313.15 K, with the maximum temperature difference not exceeding 5 K [1].

The cooling systems of power batteries in new energy vehicles are categorized into air cooling [2,3], liquid cooling [4,5], and phase change material (PCM) cooling [6–8] according to different methods. Liquid cooling is favored for its low cost and uniform temperature distribution. Inspired by the bionic fractal geometry, He Ping et al. [9] designed and optimized a battery thermal management system based on the I-channel liquid cooling plate, which resulted a reduction in the maximum temperature from 305.33 K to 303.94 K. Additionally, the standard deviation of the surface temperature and the maximum pressure were also significantly reduced. Deng et al. [10] designed a novel bionic double-layer foliated structure and used genetic algorithm to optimize the structural parameters of the liquid-cooled plate. The optimization results showed that the pressure drop decreased with the decrease in temperature difference. Fan et al. [11] designed a double-layer tree cooling plate and established the relationship between structural parameters and objective functions by combining Latin hypercube sampling with radial basis function (RBF). The simulation results showed that the maximum temperature, surface temperature difference, and pressure drop of the cooling plate were reduced by 13.29 K, 3.35 K, and 382.1 Pa, respectively. Liu Xianqian et al. [12] analyzed the influence of parameters in the bionic wing vein channel plate on cooling performance. In comparison with the parallel-flow channel plate, it was found that the bionic wing vein channel can improve the temperature uniformity of lithium-ion batteries and reduce the power loss.

The biomimetic structure of a liquid cooling plate is usually singular. In this paper, a composite biomimetic liquid cooling plate structure based on the human blood vessel branch and the insect wing vein is proposed, combined with a micro-channel to obtain better heat transfer efficiency and temperature uniformity. Through experiments and simulations, the laws between the thermal generation characteristics of batteries under dynamic working conditions, the geometric parameters of the liquid cooling plate system, and operating conditions were explored. The cooling performance and temperature uniformity were optimized to ensure that the maximum temperature of the battery was controlled below 318.15 K under a 3 C discharge rate, with the maximum temperature difference kept within 7 K.

2. Battery Heat Generation Experiment and Simulation

The heat generation and temperature characteristics of the battery were studied. The battery is a prismatic lithium-ion battery, model INP27148102A-50AH.

The charge and discharge equipment used in the experiment includes a temperature control box with voltage and current testing function, a temperature detector, etc., which mainly conducts high-/low-temperature charge/discharge testing, as well as monitoring of the voltage, current, and temperature of the experimental samples, as shown in Figure 1. By connecting the positive and negative electrodes of the experimental battery with the current collection wires and voltage collection wires of the temperature control box, T-type thermocouples are arranged in the test position of the battery. The initial temperature of the temperature detector is set to 25 degrees Celsius, and the experiment steps are set on a computer. Five T-type thermocouples are respectively arranged on the positive electrode, negative electrode, front side, bottom side, and flank of the test battery.

2.1. Internal Resistance Test of Battery Cell

Hybrid pulse power characterization (HPPC) [13] collects the voltage, temperature, and current of a single battery under the three states of charging, shelving, and discharging. The difference of current pulse tests in each group is 10%, and the voltage change curve with time is obtained. The polarization internal resistance and ohm internal resistance of the battery were calculated by the variation trend of the battery voltage [14]. The voltage response curve of a pulse discharge is extracted from it, as shown in Figure 2.

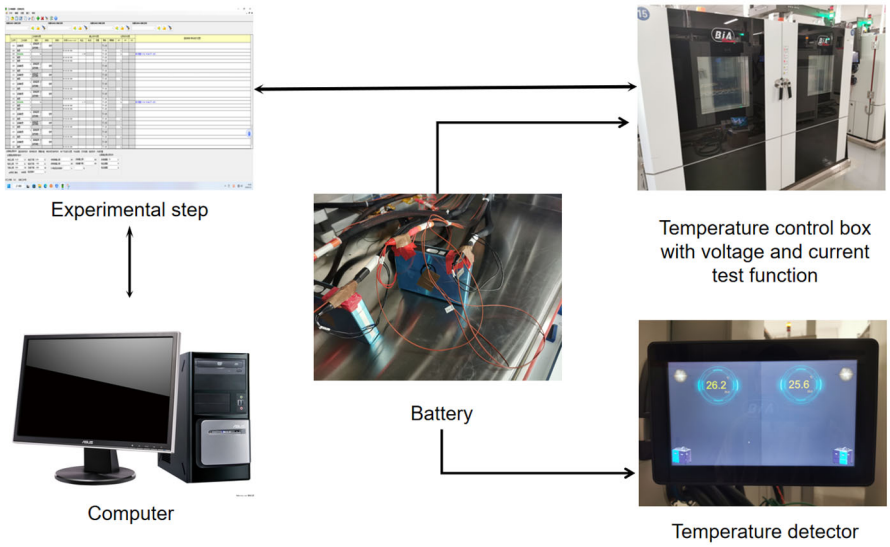

Figure 1. Experimental process.

$$R_n = \frac{U_A - U_B}{I} \tag{1}$$

$$R_P = \frac{U_B - U_C}{I} \tag{2}$$

$$R = R_n + R_P \tag{3}$$

where R is the internal resistance of the battery; R_n is the ohmic internal resistance of the battery; R_p is the polarization internal resistance of the battery, unit mΩ; I is the discharge current of the battery, unit A; and the corresponding voltage from U_A drops to U_B. U_A is the voltage change caused by the internal resistance of the battery, and the voltage drop from U_B to U_C is the voltage change caused by the internal resistance of the battery polarization.

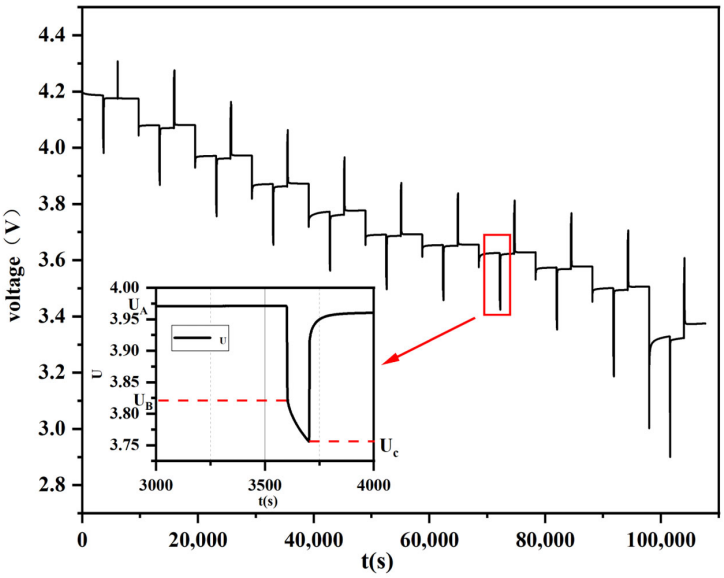

Figure 2. Overall voltage curve of HPPC experiment.

According to the above calculation formula, during the HPPC experiment, the battery voltage parameters under different *SOC* states were identified, and then the total internal resistance was calculated.The internal resistance is shown in Table 1 below.

Table 1. Total internal resistance of batteries with different discharge rates under different *SOC*.

SOC	0.5C Discharge Resistance (mΩ)	1C Discharge Resistance (mΩ)	2C Discharge Resistance (mΩ)	3C Discharge Resistance (mΩ)
1	1.104	1.128	1.135	1.103
0.9	1.097	1.128	1.119	1.108
0.8	1.083	1.106	1.080	1.098
0.7	1.100	1.102	1.100	1.095
0.6	1.079	1.079	1.077	1.086
0.5	1.032	1.048	1.062	1.070
0.4	1.052	1.058	1.064	1.077
0.3	1.068	1.071	1.080	1.100
0.2	1.103	1.112	1.126	1.165
0.1	1.201	1.224	1.292	1.467
0	1.694	2.298	1.882	2.062

Through the polynomial fitting of resistance parameters in MATLAB2022, the fifth-order curve has the highest degree of fitting, and the fitting error is within the allowable range. Taking 3 C as an example, the discharge internal resistance and *SOC* can be fitted as

$$R = (2.064 - 8.432SOC + 27.64SOC^2 - 43.82SOC^3 + 33.91SOC^4 - 10.26SOC^5)/1000 \quad (4)$$

where R is the discharging resistance of 3 C, and *SOC* is the state of charge.

The calculation formula of *SOC* is

$$SOC = 1 - \frac{It}{3600C} \quad (5)$$

where 1 represents that *SOC* in the initial state is 1, I is the discharge current (unit: A), t is the discharge time (unit: s), and C indicates the actual capacity of the battery (unit: Ah).

The relationship between the internal resistance of the experimental battery and the state of charge was obtained by fitting the internal resistance, as shown in Figure 3.

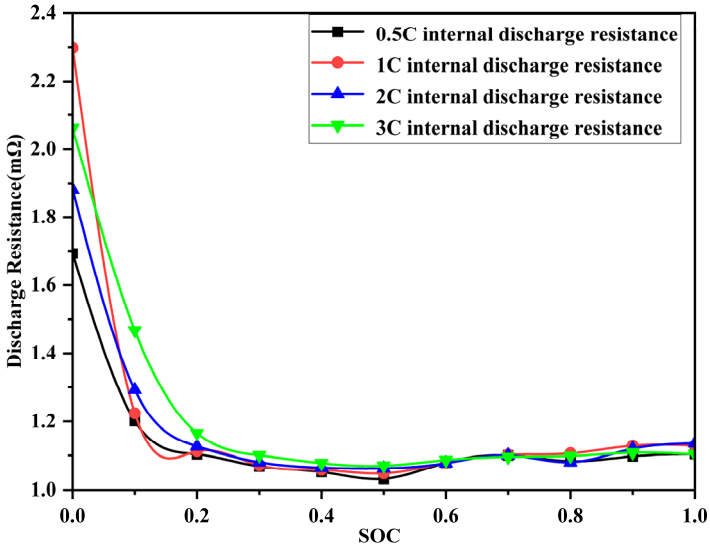

Figure 3. Fitting curve of battery internal resistance and *SOC*.

2.2. Battery Heat Production Rate Model

Accurate calculation of the battery heat production rate is the basis of battery thermal management system design and analysis. The heat production rate of cell is affected by many factors such as current density, charging state, and ambient temperature, which is highly nonlinear and difficult to measure accurately.

Since this study did not consider the effects of capacitive and induced reactance in the battery on the temperature rise of the battery, the simplified Bernadi D [8], heat generation model was adopted in this paper, and the heat generation rate of the battery during discharge can be obtained by the following formula:

$$q = \frac{1}{V}[I^2R + IT\frac{\partial U}{\partial T}] \quad (6)$$

where q represents the heat generation rate per unit volume of the battery, unit W/m^3; V is the volume of the battery, unit m^3; I indicates the current when the battery discharges, unit A; R is the internal discharge resistance of the battery, unit mΩ; T is the working temperature, unit K; and $\partial U/\partial T$ is the unit of the temperature entropy coefficient V/K.

2.3. Temperature Entropy Coefficient Fitting

The voltage parameters of the battery under different *SOC* discharge conditions at different temperatures were measured by an HPPC experiment, and the accurate temperature entropy coefficient was obtained by fitting the voltage parameters. The temperature entropy coefficient of the last second voltage and temperature recorded at different temperatures is obtained by a linear fitting. The temperature entropy coefficient of each *SOC* state is calculated by this method, and then the temperature entropy coefficient of each *SOC* state is fitted five times. The temperature entropy coefficient and *SOC* can be fitted as

$$\begin{aligned}\partial U/\partial T = {} & (0.0001414 - 0.00001075SOC + 0.0000005422SOC^2 \\ & - 0.00000001088SOC^3 + 0.0000000001108SOC^4 - 0.0000000000004721SOC^5)\end{aligned} \quad (7)$$

By importing the fitted temperature entropy coefficient and discharge internal resistance into fluent through UDF, the temperature rise of the battery under dynamic working conditions is simulated.

Figure 4 shows the relationship between the temperature entropy coefficient and the state of charge. According to the image, the temperature entropy coefficient ranges from −0.5 to 0.2 mV/K. When *SOC* is between 0.1 and 0.7, the temperature entropy coefficient shows an upward trend; when *SOC* is between 0.7 and 1, the temperature entropy coefficient shows an overall downward trend.

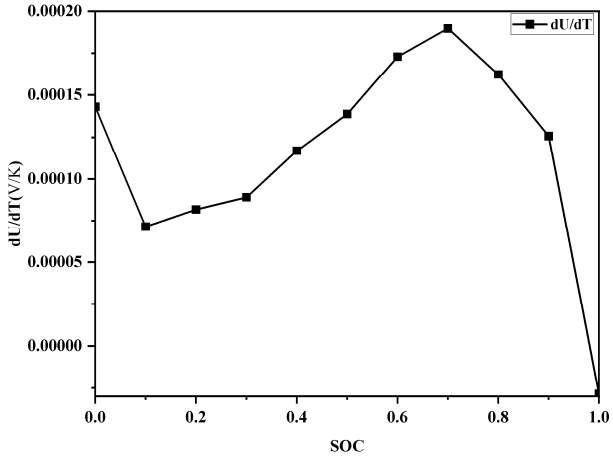

Figure 4. The fitting curve of temperature entropy coefficient and state of charge.

2.4. Experimental Error Analysis

In order to ensure the accuracy of experimental data, uncertainty is divided into Class A uncertainty and Class B uncertainty according to different evaluation methods. Through multiple measurements, Class A uncertainty is estimated by statistical methods and Class B uncertainty is estimated by non-statistical methods. Class A uncertainty conforms to a distribution and is represented by experimental error. Class B uncertainty is the minimum

error value of the measuring instrument, and the measurement result includes Class A uncertainty and Class B uncertainty. The synthetic standard uncertainty is used to represent the uncertainty of multiple sources of uncertainty affecting the measurement result.

$$\mu_A = \sqrt{\frac{\sum_{i=1}^{n} (S_i - \overline{S})^2}{(n-1)n}} \tag{8}$$

$$\mu_B = \frac{\Delta}{C} \tag{9}$$

$$\mu_c = \sqrt{\sum_{i=1}^{m} (\mu_{Ai})^2 + \sum_{j=1}^{n} (\mu_{Bj})^2} \tag{10}$$

The uncertainty of the main parameters of the experiment is shown in Table 2.

Table 2. The uncertainty of the main parameters of the experiment.

Parameter	Uncertainty
Temperature (T-type thermocouple)	±0.2
Voltage (V)	±0.4
Current (A)	±0.2
Internal resistance (mΩ)	0.1%

2.5. Battery Heat Generation Simulation

The simulation calculation of the maximum surface temperature of a single battery at four discharge rates of 0.5C, 1C, 2C, and 3C is compared with the temperature rise experiment. The results are shown in Figure 5. The simulation temperature rise results of the battery are basically consistent with those obtained in the temperature rise experiment. The maximum surface temperature is 29.1 °C, 32.8 °C, 43.1 °C, and 56.5 °C, respectively. Compared with the corresponding simulation results, the maximum temperature difference during discharge is 2.0 °C, 1.4 °C, 0.8 °C, and 1.8 °C, respectively. The temperature difference is less than 2 °C, which fully indicates that the numerical simulation of the battery temperature field thermal model used in this paper can well reflect the actual heat generation of lithium-ion power batteries.

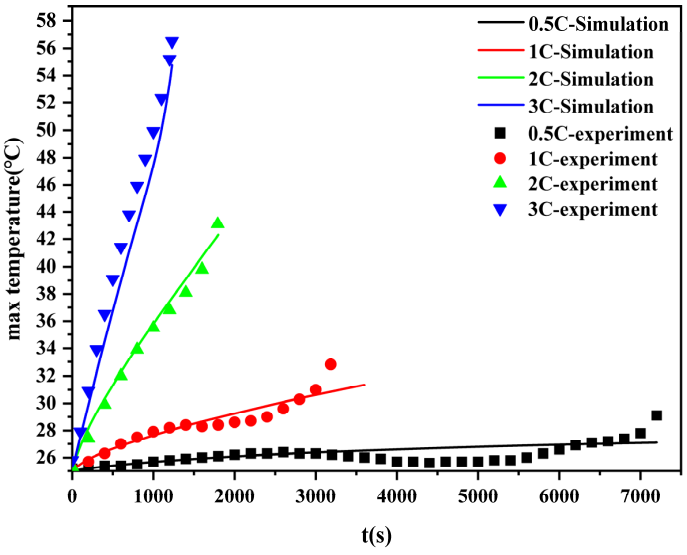

Figure 5. Thermal model verification of single cells.

3. New Bionic Power Battery Liquid Cooling System Model

3.1. Design and Modeling of Liquid Cooling Plate

The experimental battery is composed of three INP27148102A-50AH prismatic lithium-ion cells connected in series, and a liquid cooling plate is placed between each two prismatic batteries to cool the battery. The size of the lithium-ion battery is 148 mm × 26 mm × 97 mm, the positive pole size is 20 mm × 20 mm × 3 mm, and the negative pole size is 22 mm × 20 mm × 3 mm. Compared with traditional single biomimetic structures of liquid cooling plates, the liquid cooling plate structure designed in this paper possesses two biomimetic characteristics: insect wing veins and blood vessels. The liquid cooling plate flow path is designed according to the distribution of human blood vessel branches and the structure of insect wing veins to improve the uniformity of battery temperature. The branch structure of insect wing veins [15,16] has the characteristics of low flow resistance and high transmission efficiency. Therefore, based on the wing vein structure, the basic frame of bionic liquid-cooled plate micro-channel is constructed. The cross-section structure of blood vessel can reduce the loss of blood flow rate and reduce the energy loss. According to this feature, the arc drag reducing structure of the cross section of the micro-channel is designed to form the liquid-cooled micro-channel with the complex bionic structure of wing vein and blood vessel. The external dimension of the liquid cooling plate is 152 mm × 100 mm × 6 mm (length × width × height). The layout is shown in Figure 6. The geometric structure is shown in Figure 7. The flow channel is composed of six-level parting flow channels. The liquid enters the main flow channel from the entrance and then enters the middle parting flow channel again, and finally gathers into the main flow channel and is discharged from the outlet 148 mm × 96 mm × 4 mm. The section length and width of the inlet and outlet flow path and the liquid cooling plate are 7 mm and 4 mm, and the angle between the inlet and the cold end cold plate is 146.92° and 123.08°, respectively.

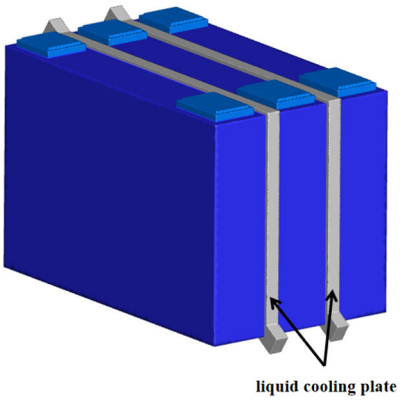

Figure 6. Liquid cooling geometric model of battery module.

The flow channel parameters of the liquid cooling plate with biomimetic biological structure are satisfied:

$$A = \frac{L_{K+1}}{L_K} \tag{11}$$

$$B = \frac{P_{K+1}}{P_K} \tag{12}$$

where L_K and P_K are the length and the width of each throttling channel, respectively; for example, L_1 is the length of the first throttling channel, P_1 is the width of the first throttling channel, and A and B are the ratio of the length and the width of the k + 1 throttling channel and the k throttling channel, respectively, both of which are 0.8. From top to bottom, the flow path is defined as one to seven levels, from the middle fourth stage to both sides, and the first section length L_1 of each level of the flow path is 20, 14, 8, and 5, respectively. The widths P_1 are 5, 5, 4, and 2, respectively. M and W represent

the connection arc radius between two flow channels, where M is the branch diffusion section, and W is the branch aggregation section. For example, M_4 is the connection arc radius between the first and second sections of the fourth section, and M_{41} and M_{42} are the connection arc radius between the third and fourth sections of the fourth section of the fourth section. M_1 to M_7 are 0.2, 0.4, 0.6, 0.8, 0.6, 0.4, and 0.2, respectively. M_{11}, M_{21}, M_{22} to M_{72} are 0.2, 0.2, 0.4, 0.4, 0.6, 0.6, 0.4, 0.4, 0.4, 0.2, and 0.2, respectively. W_4 is the connection arc radius between the eighth and ninth sections of the fourth-stage runner; similarly, W_{41} and W_{42} are the connection arc radius between the third and fourth sections of the fourth stage runner, respectively. The corresponding M and W sizes are the same.

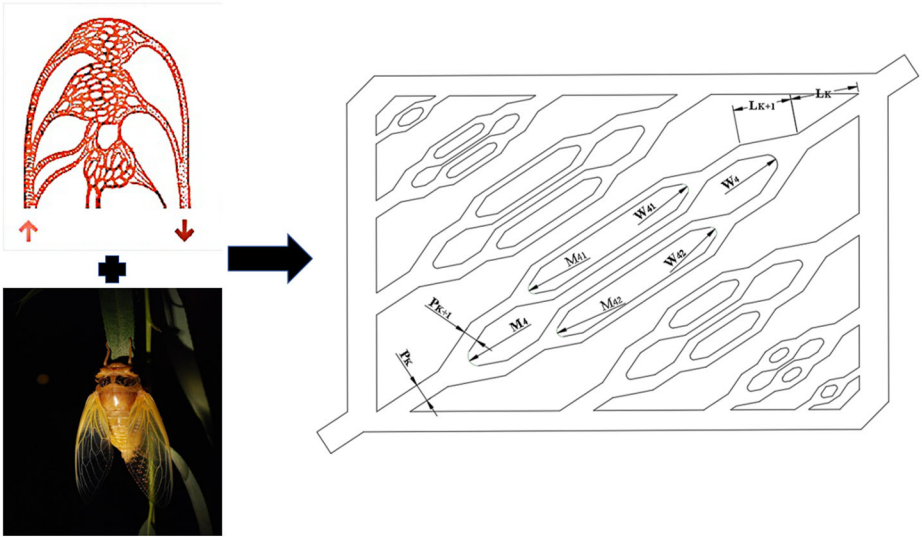

Figure 7. Liquid cooling plate model structure of biomimetic organism.

3.2. Physical Property Parameters

The cathode material of the battery is lithium nickel–cobalt manganese. In order to consider the subsequent high- and low-temperature test, and water will freeze at low temperature, the coolant is adopted with a concentration of ethylene glycol solution with a volume concentration of 50%. The physical property parameters of the prismatic-shell lithium-ion monomer battery and the coolant are shown in Table 3.

Table 3. The physical property parameters of battery and the coolant.

Project	Density/(kg/m^3)	Specific Heat Capacity/[J/(kg·K)]	Thermal Conductivity/[W/(m·K)]
Coolant	1071	3300	0.384
Battery	2355	1070	Height direction 17.2 Width direction 5.3 Length direction 23.4

3.3. Model Governing Equation

To simplify the calculation, the following assumptions are used.

(1) The density of the liquid cooling plate is uniform, and the heat transfer direction is the same.
(2) The liquid is incompressible and flows stably [17].
(3) The coolant in the flow channel has a uniform flow path, and the physical properties of aluminum and 50% ethylene glycol are temperature-independent [18].

It is assumed that the energy governing equation of the liquid cooling plate is as follows [19]:

$$\frac{\partial}{\partial r}\left(\rho_{lcp} c_{lcp} T_{lcp}\right) = -\nabla\left(\lambda_{lcp} \nabla T_{lcp}\right)\tau \tag{13}$$

where ρ_{lcp}, c_{lcp}, T_{lcp}, and λ_{lcp} are the density, specific heat capacity, temperature, and thermal conductivity of the liquid-cooled plate, respectively.

The mass and control equations of the coolant are as follows [20]:

Mass conservation equation (or continuity equation):

$$\nabla\cdot\left(\rho_w \vec{v}\right) = 0 \tag{14}$$

conservation of momentum:

$$\rho_w\left(\vec{v}\cdot\nabla\cdot\vec{v}\right) + \nabla\cdot\mathrm{p} = \mu\nabla^2\vec{v} \tag{15}$$

conservation of energy:

$$\rho_w c_w\left(\vec{v}\cdot\nabla T_w\right) = k_w\nabla^2 T_w \tag{16}$$

where ρ_w, $\vec{v}$, p, μ, c_w, T_w, and k_w represents the coolant density, motion vector, static pressure, dynamic viscosity, specific heat capacity, temperature, and thermal conductivity, respectively.

3.4. Boundary Conditions and Parameter Settings

The flow heat transfer of the power battery module with a bionic liquid cooling plate structure was solved by using ANSYS FLUENT 2022R2 transient simulation. The coolant is a 50% glycol solution by volume. The inlet of the flow channel is set as the velocity inlet, the temperature is 273.15 K, and the flow velocity is 0.2 m/s, 0.4 m/s, 0.6 m/s, 0.8 m/s, and 1 m/s. The corresponding Reynolds numbers are 321.26, 643.23, 964.84, 1286.46, and 1608.07, respectively, all of which are less than 2300, and the flow type is laminar flow. The outlet is the pressure outlet, and the pressure is set to standard atmosphere. In order to improve the accuracy of the simulation, five boundary layers were added to the fluid–solid junction between the fluid domain and the liquid cooling plate, and the boundary layer was encrypted. The fluid–structure coupling interface is adopted on the surface of the runner and is set as the no-slip boundary. The lithium-ion battery module and the air environment are convection heat transfer, the convection heat transfer coefficient is set to 5 W(m^2*K), and the ambient temperature is 298.15 K. Coupled algorithm was adopted for the coupling method of pressure and velocity. The pressure, momentum, and energy equations adopted the second-order upwind format with the default relaxation factor. The step size was 1 s, and the total step size was 1200.

3.5. Calculation Domain Meshing and Grid Independence Verification

In the simulation process, grid independence verification is carried out to balance calculation accuracy and calculation time. The grid with the total number of 1,910,417, 2,558,080, 4,181,876, 6,983,129, and 7,021,073 is simulated at a discharge rate of 3 C and a step size of 1200 s. When the number of grids is 2,558,080, the number of grids increases, and the maximum temperature and temperature difference on the surface of the battery module no longer change.

4. Simulation Results and Analysis

In order to study the heat dissipation performance of the bionic structure of the liquid cooling plate in the battery module, the maximum surface temperature of the battery module after the discharge of the battery modules by a 3 C discharge rate was used as an evaluation criterion, including the maximum temperature, maximum temperature difference, and inlet and outlet pressure drop of the liquid cooling plate.

4.1. Influence of Liquid Flow Rate

By analyzing the maximum temperature of the battery module, maximum temperature difference, and pressure drop at the inlet and outlet of the liquid-cooled plate model, in order to further optimize the model, a new evaluation index, the power of the pump, is introduced:

$$P_W = V_{in} A_{in} \Delta P \tag{17}$$

where V_{in} is the inlet flow rate, unit m/s; A_{in} is the area of import, unit m^2; and ΔP is the pressure drop at the inlet and outlet, unit Pa.

Generally, for measures to strengthen heat transfer, the flow resistance will increase with the increase in flow. Considering the comprehensive heat transfer and resistance characteristics, the ratio of the heat transfer factor to the resistance coefficient is taken as the evaluation index of comprehensive performance.

$$PEC = \frac{j}{f} \tag{18}$$

where $j = \frac{h}{\rho U c_p} \mathrm{P}\gamma^{2/3}$ and $f = \frac{2\Delta pL}{\rho U^2 D}$.

The pump power change curves of the maximum surface temperature, maximum surface temperature difference, inlet and outlet pressure difference, and consumption of the battery modules at different flow rates are shown in Figure 8. It can be seen from Figure 8a that with the increase in the flow rate, the maximum surface temperature of the battery modules gradually decreases, successively to 306.43 K, 305.71 K, 305.45 K, 305.31 K, and 305.22 K. At the same time, the maximum temperature difference of the battery modules gradually decreased and was given as 7.71 K, 7.25 K, 7.08 K, 6.99 K, and 6.92 K, respectively. The import and export pressure drop gradually increased in order of 18.98 Pa, 68.76 Pa, 146.08 Pa, 245.71 Pa, and 372.59 Pa, respectively. This is because the flow rate is increasing at the same time; the pressure of the liquid on the inlet is also increasing.

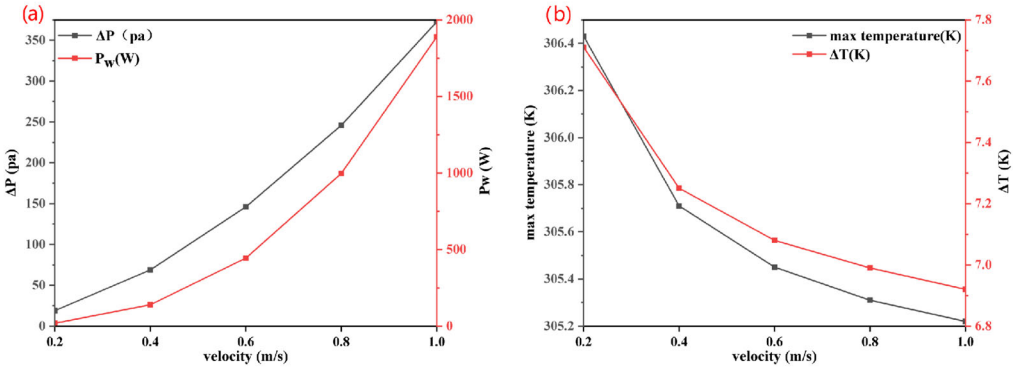

Figure 8. Effect of liquid flow rate on system performance: (**a**) pressure difference and pump power; (**b**) max temperature and temperature difference.

When the liquid flow rate is less than 0.6 m/s, the maximum temperature and maximum temperature difference on the battery surface rapidly drop, and when the flow rate continues to increase, the cooling effect gain caused by the flow rate decreases, and the pressure loss at the inlet and outlet increases by 126.88 Pa.

When the liquid flow rate is less than 0.6 m/s, the pump power consumed is 19.25, 139.45, which increased by 120.2; when the liquid flow rate is greater than 0.6 m/s, the pump power consumed is 996.61, 1889.05, which increased by 892.39. At this time, the maximum temperature of the battery is only 305.45 K, although when the liquid flow rate is greater than 0.6 m/s, the maximum temperature and maximum temperature difference on the surface of the battery are decreasing, but the pressure difference between the inlet and outlet and the pump power consumed are also gradually increasing. The goal of strengthening heat transfer is not only to enhance heat transfer but also to make its resistance as small

as possible, and the comprehensive performance of the system is better at this time. In order to obtain a higher PEC value, when the Reynolds number is lower than 1000, that is, the liquid flow rate is less than 0.6 m/s, the value of PEC gradually increases; when the Reynolds number is greater than 1000, the value of PEC gradually decreases. At this time, it can be found that the system obtains the highest heat transfer performance when the flow rate is 0.6 m/s. With the increase in the heat transfer factor and the decrease in the resistance coefficient, higher comprehensive performance can be obtained. Compared with the above results, it is found that the system with liquid flow rate of 0.6 m/s has the best comprehensive heat transfer performance.

4.2. Influence of Contact Arc Radius between Flow Channels

Through the simulation of the bionic liquid cooled plate structure model, it is found that the flow rate loss occurs when liquid flows from the pipeline to each secondary flow channel; mainly due to the angle between the sharp impact of the liquid, the liquid disperses into the secondary flow channel, resulting in a reduced flow rate. In order to analyze the impact of the contact arc radius between different flow channels on the system performance, three Scenarios are designed. For M_4, 0.8, 1.5, and 2.5, and for M_{21} to M_{41}, 0.6, 1, and 1.5, respectively, the contact arc radius from M_1 to M_7 in Scenario one is 0.2, 0.4, 0.6, 0.8, 0.6, 0.4, and 0.2, respectively. The contact arc radius of the secondary runner from M_1 to M_7 is 0.2, 0.2, 0.4, 0.4, 0.6, 0.6, 0.4, 0.4, 0.2, and 0.2, respectively. In Scenario two, the contact arc radius from M_1 to M_7 is 0.4, 0.6, 0.8, 1.5, 0.8, 0.6, and 0.4, respectively. The contact arc radius of the secondary runner M_1 to M_7 is 0.4, 0.4, 0.6, 0.6, 1, 1, 0.6, 0.6, 0.4, and 0.4, respectively. The contact arc radius of Scenario three from M_1 to M_7 is 0.8 1, 1.2, 2.5, 1.2, 1, and 0.8, respectively. The contact arc radius of the secondary runner M_1 to M_7 is 0.8, 0.8, 1, 1, 1.5, 1.5, 1, 1, 0.8, and 0.8, respectively. The three Scenarios are simulated under the flow rates of 0.2 m/s, 0.4 m/s, 0.6 m/s, 0.8 m/s, and 1 m/s, and the results are shown in Figure 9. Figure 9 shows the influence of the contact arc radius between different flow channels on system performance. It can be seen from Figure 9a,b that the simulation results of the maximum surface temperature and maximum temperature difference of the battery modules of the three Scenarios gradually decrease, with the maximum temperature decreasing from 306.4 K to 305 K and the maximum temperature difference from 7.7 K to 6.7 K.

Under the same flow rate, the maximum surface temperature and maximum temperature difference of the battery module gradually decrease with the increase in the contact arc between the flow channels. However, after 0.4 m/s, there is basically no difference between the maximum surface temperature and maximum temperature difference of the battery module in Scenario two and Scenario three, while compared with Scenario one, the maximum surface temperature difference, maximum temperature difference, and pressure difference of the inlet and outlet significantly decrease. The pump power consumed by the three Scenarios at different flow rates is basically the same, which indicates that the increase in the contact arc radius between the flow channels will reduce the pressure loss in the flow channels and further improve the heat dissipation performance of the system. Figure 10 shows the pressure and temperature cloud diagram of the liquid cooling plate with biomimetic biological structure under the flow rate of 0.2 m/s of the three Scenarios. The pressure at the inlet is optimized and decreases as a whole, especially the pressure distribution in the uppermost flow channel. The pressure distribution in the flow channel of Scenario three is basically not much different from that of Scenario two, indicating that the increase in the contact arc radius no longer causes too much influence on the optimization of the system. In summary, it shows that increasing the contact arc of the flow channel is beneficial to reducing the pressure of the system.

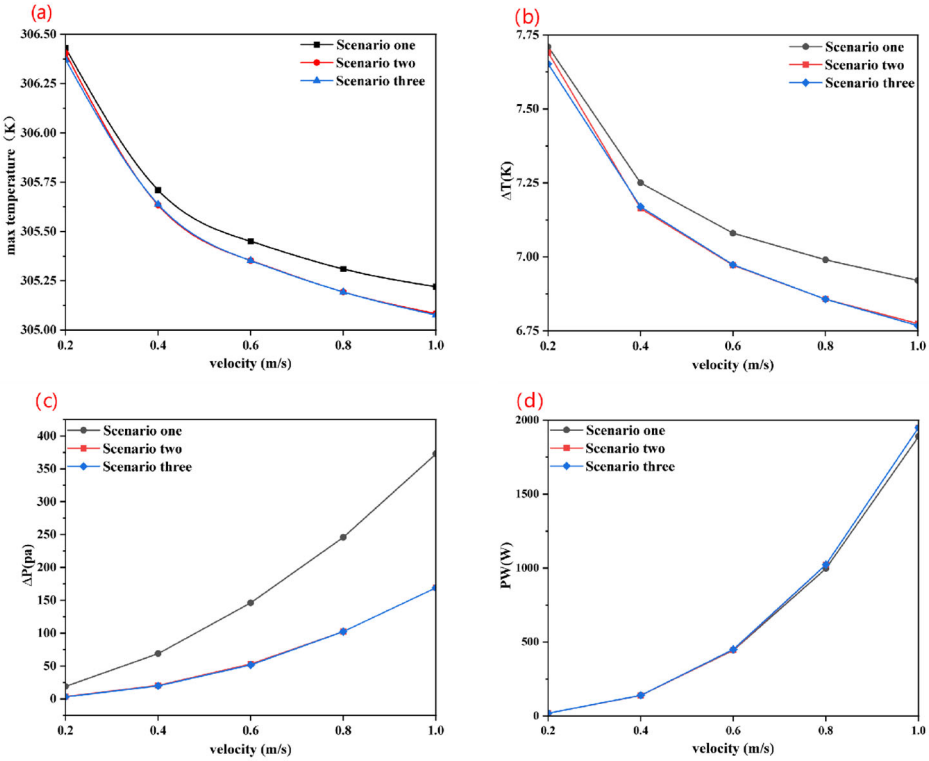

Figure 9. Effect of angular arcs between runners on system performance: (**a**) maximum surface temperature; (**b**) temperature difference; (**c**) pressure difference; and (**d**) pump power.

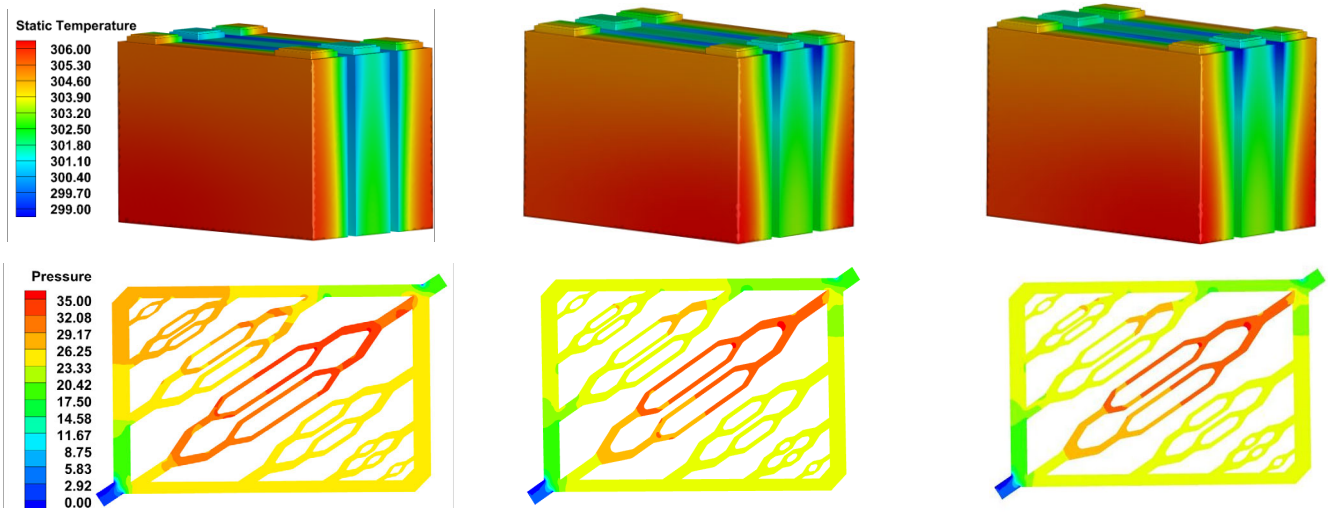

Figure 10. Pressure and temperature cloud images of the three Scenarios.

5. Conclusions

This study introduces an innovative biomimetic liquid cooling plate for prismatic lithium-ion batteries, drawing inspiration from the intricate structures of human blood vessels and insect wing veins. The experimental battery's ohmic internal resistance and temperature entropy coefficient were meticulously predicted through hybrid pulse power characterization (HPPC) experiments. Subsequently, numerical simulations were conducted to assess the heat transfer efficacy of the cooling plate under dynamic conditions, focusing on the coolant flow rate across the battery and the contact arc radius between the micro-channels. The findings are as follows:

1. The maximum surface temperature of the battery modules decreases with increasing flow velocity, particularly pronounced from 0.2 m/s to 0.6 m/s, where it drops

from 306.43 K to 305.45 K. The inlet and outlet pressure difference also slightly elevates, from 30.37 Pa to 68.72 Pa. Beyond a flow velocity of 0.6 m/s, the temperature reduction is less pronounced, and the pressure difference significantly increases from 146.08 Pa to 372.59 Pa, leading to greater energy loss. Hence, a flow rate of 0.6 m/s is deemed optimal.

2. Enlarging the contact arc radius between flow channels at liquid flow rates ranging from 0.2 m/s to 1 m/s, with values of 0.8, 1.5, and 2.5, results in a significant reduction in the system's maximum surface temperature. Notably, when the contact arc radius is 0.8, the temperature drops from 306.43 K to 305.22 K. Further increments to 1.5 and 2.5 yield even more substantial decreases, enhancing the heat transfer performance of the system and increasing the pressure difference across the system, indicating that optimizing the contact arc radius is instrumental in achieving superior thermal management. The study conclusion underscores the potential of biomimetic design in enhancing the thermal management of lithium-ion batteries, offering a promising direction for future research and development in the field.

Author Contributions: Conceptualization, formal analysis, writing—review and editing, funding acquisition, C.W., methodology, software, writing—original draft preparation, data curation, Z.W., funding acquisition, formal analysis, Z.L., data curation, resources, D.L., writing—review and editing, X.Q. All authors have read and agreed to the published version of the manuscript.

Funding: This research was funded by [Key R&D Program of Changzhou], grant number [CE20230021], and Postgraduate Research & Practice Innovation Program of Jiangsu Province, grant number [SJCX23_1610].

Data Availability Statement: The original contributions presented in the study are included in thearticle, further inquiries can be directed to the corresponding author.

Conflicts of Interest: Dinghong Liu, Zhaoyang Li and Xin Qi are employees of CATARC Automotive Test Center (Changzhou) Co., Ltd. The paper reflects the views of the scientists, and not the company.

References

1. Wu, W.; Wang, S.; Wu, W.; Chen, K.; Hong, S.; Lai, Y. A critical review of battery thermal performance and liquid based battery thermal management. *Energy Convers. Manag.* **2019**, *182*, 262–281. [CrossRef]
2. Widyantara, R.D.; Naufal, M.A.; Sambegoro, P.L.; Nurprasetio, I.P.; Triawan, F.; Djamari, D.W.; Nandiyanto, A.B.D.; Budiman, B.A.; Aziz, M. Low-cost air-cooling system optimization on battery pack of electric vehicle. *Energies* **2021**, *14*, 7954. [CrossRef]
3. Saechan, P.; Dhuchakallaya, I. Numerical investigation of air cooling system for a densely packed battery to enhance the cooling performance through cell arrangement strategy. *Int. J. Energy Res.* **2022**, *46*, 20670–20684. [CrossRef]
4. Zhao, G.; Wang, X.; Negnevitsky, M.; Li, C. An up-to-date review on the design improvement and optimization of the liquid-cooling battery thermal management system for electric vehicles. *Appl. Therm. Eng.* **2023**, *219*, 119626. [CrossRef]
5. Zhang, F.; Huang, Z.; Li, S.; Sun, S.; Zhao, H. Design and thermal performance analysis of a new micro-fin liquid cooling plate based on liquid cooling channel finning and bionic limulus-like fins. *Appl. Therm. Eng.* **2024**, *237*, 121597. [CrossRef]
6. Rao, Z.; Qian, Z.; Kuang, Y.; Li, Y. Thermal performance of liquid cooling based thermal management system for cylindrical lithium-ion battery module with variable contact surface. *Appl. Therm. Eng.* **2017**, *123*, 1514–1522. [CrossRef]
7. Luo, J.; Zou, D.; Wang, Y.; Wang, S.; Huang, L. Battery thermal management systems (BTMs) based on phase change material (PCM): A comprehensive review. *Chem. Eng. J.* **2022**, *430*, 132741. [CrossRef]
8. Bernardi, D.; Pawlikowski, E.; Newman, J. A general energy balance for battery systems. *J. Electrochem. Soc.* **1985**, *132*, 5. [CrossRef]
9. He, P.; Lu, H.; Fan, Y.; Ruan, H.; Wang, C.; Zhu, Y. Numerical investigation on a lithium-ion battery thermal management system utilizing a double-layered I-shaped channel liquid cooling plate exchanger. *Int. J. Therm. Sci.* **2023**, *187*, 108200. [CrossRef]
10. Deng, T.; Ran, Y.; Yin, Y.; Chen, X.; Liu, P. Multi-objective optimization design of double-layered reverting cooling plate for lithium-ion batteries. *Int. J. Heat Mass Transf.* **2019**, *143*, 118580. [CrossRef]
11. Fan, Y.; Wang, Z.; Fu, T. Multi-objective optimization design of lithium-ion battery liquid cooling plate with double-layered dendritic channels. *Appl. Therm. Eng.* **2021**, *199*, 117541. [CrossRef]
12. Liu, X.; Sun, A.; Chuan, T. Research on liquid cooling and heat dissipation of lithium-ion battery pack based on bionic wings vein channel cold plate. *Energy Storage Sci. Technol.* **2022**, *11*, 2266. [CrossRef]
13. Zhan, S.; Liang, L.; Li, Z.; Yu, C.; Wang, F. Topology optimization of liquid cooling plate for lithium battery heat dissipation based on a bionic leaf-vein structure. *Int. J. Heat Mass Transf.* **2024**, *231*, 125898. [CrossRef]

14. Zhan, S.; Que, Y.; Yin, Y.; Li, Z.; Yu, C. A novel tree-like bionic structure for liquid-cooled lithium-ion battery plates. *Int. J. Therm. Sci.* **2024**, *203*, 109098. [CrossRef]
15. Li, B.; Mao, Z.; Song, B.; Lu, C.; Tian, W.; Zhang, B. Study on battery thermal management of autonomous underwater vehicle by bionic wave channels with liquid cooling. *Int. J. Energy Res.* **2021**, *45*, 13269–13283. [CrossRef]
16. Tondeur, D.; Luo, L. Design and scaling laws of ramified fluid distributors by the constructal approach. *Chem. Eng. Sci.* **2004**, *59*, 1799–1813. [CrossRef]
17. Chen, S.; Peng, X.; Bao, N.; Garg, A. A comprehensive analysis and optimization process for an integrated liquid cooling plate for a prismatic lithium-ion battery module. *Appl. Therm. Eng.* **2019**, *156*, 324–339. [CrossRef]
18. Sheng, L.; Su, L.; Zhang, H.; Li, K.; Fang, Y.; Ye, W.; Fang, Y. Numerical investigation on a lithium ion battery thermal management utilizing a serpentine-channel liquid cooling plate exchanger. *Int. J. Heat Mass Transf.* **2019**, *141*, 658–668. [CrossRef]
19. Wang, C.; Zhang, G.; Meng, L.; Li, X.; Situ, W.; Lv, Y.; Rao, M. Liquid cooling based on thermal silica plate for battery thermal management system. *Int. J. Energy Res.* **2017**, *41*, 2468–2479. [CrossRef]
20. Mandelbrot, B. How Long Is the Coast of Britain? Statistical Self-Similarity and Fractional Dimension. *Science* **1967**, *156*, 636–638. [CrossRef] [PubMed]